Magnetic Resonance Studies and Molecular Orbital Calculations on the Doublet and Triplet States of Bacteriopurpurin: a Potential Second-Generation Photosensitizer for Photodynamic Therapy

Christopher W. M. Kay,* Fosca Conti, Michael Fuhs, Martin Plato, and Stefan Weber

Institute of Experimental Physics, Free University Berlin, 14195 Berlin, Germany

Enrica Bordignon and Donatella Carbonera

Department of Physical Chemistry, University of Padova, 35131 Padova, Italy

Byron C. Robinson

Miravant Medical Technologies, Santa Barbara, California 93117

Mark W. Renner and Jack Fajer

Energy Sciences and Technology Department, Brookhaven National Laboratory, Upton, New York 11973

Bacteriopurpurin is a macrocyclic compound at the saturation level of bacteriochlorins that was specifically synthesized as a potential photosensitizer in photodynamic therapy. It exhibits a long-wavelength Q_y absorption band at 843 nm, which is a necessary prerequisite for a deep tissue penetration. Magnetic resonance spectroscopic properties of bacteriopurpurin have been examined by fluorescence-detected magnetic resonance (FDMR) and electron paramagnetic resonance (EPR) in conjunction with molecular orbital calculations. The electronic structure of the radical cation state obtained by oxidation of bacteriopurpurin with iodine is mapped by the determination of isotropic proton hyperfine coupling constants from electron−nuclear double-resonance spectroscopy at 298 K. A tentative assignment of the couplings to the various proton positions in the molecule is achieved by comparison of the experimental values with simulated ones based on semiempirical intermediate neglect of differential overlap calculations and density functional theory. The triplet-state electronic structure of the ground-state trans-configured bacteriopurpurin is characterized by the determination of the zero-field splitting parameters which represent sensitive probes for the geometric structure of the molecule. The $|D|$ and $|E|$ values obtained from time-resolved EPR (24.4 and 5.4 mT) are in favorable agreement with the respective values obtained from FDMR (24.0 and 5.3 mT). By both techniques, the presence of additional photoexcited triplet states has been confirmed. It is assumed that they arise from higher-energy tautomers of bacteriopurpurin. Their occurrence is discussed in terms of a photoinitiated intramolecular one-proton transfer from either ring II or ring IV of the trans-configured ground state to ring I or ring III to form one of the cis-configured bacteriopurpurins.

1. Introduction

The crucial role of bacteriochlorophylls (BChl) in photosynthetic energy[1−4] and electron transfer,[5,6] as well as the shifts of their Q_y transitions to the near-infrared region, have recently focused attention on bacteriochlorins (BC) as potential photosensitizers for photodynamic therapy (PDT).[7] This medical treatment employs a combination of light, porphyrin derivatives, and oxygen to induce necrotic effects on targeted cancerous and other diseased tissues.

The advantages of BCs include the bathochromic shift of the Q_y bands, which allows deeper tissue penetration of the exciting light, and the fact that photoexcited BCs can potentially function as generators of singlet oxygen via triplet states (type II photoprocess) as well as induce electron transfer (type I) because they are easily oxidized to π cation radicals. Two BCs recently

investigated consist of a BChl*a*−serine complex[8] and a BChl *a* derivative, BC*a*,[9] which absorb light in the 760−780 nm region. A considerable effort is now devoted to additional second-generation photosensitizers with tailored light-absorption properties such as the purpurins, porphyrins with annelated cyclopentenyl rings which are formally at the saturated level of chlorins and typically absorb light in the 650−715 nm region.[7,10−14] One of these, dichloro-tin(IV)etiopurpurinethylester, is in phase III clinical trials for treatment of macular degeneration of the eye.

Recently, Robinson et al.[15,16] have prepared bacteriopurpurins (**BP**), at the saturation level of BCs, which exhibit desirable Q_y absorption bands in the 840−860 nm region, some of the most bathochromic shifts for any monomeric BC. (Recall that photosynthetic light-harvesting and reaction center protein complexes utilize dimers and larger multichromophore arrays to achieve similar spectral characteristics in the 850−875 nm region.[1−6]) The authors described the spectral and redox properties of **BP** and characterized the ground-state configura-

* To whom correspondence should be addressed. Phone: +49 (30) 838-53394. FAX: +49 (30) 838-56046. E-mail: Chris.Kay@physik.fu-berlin.de.
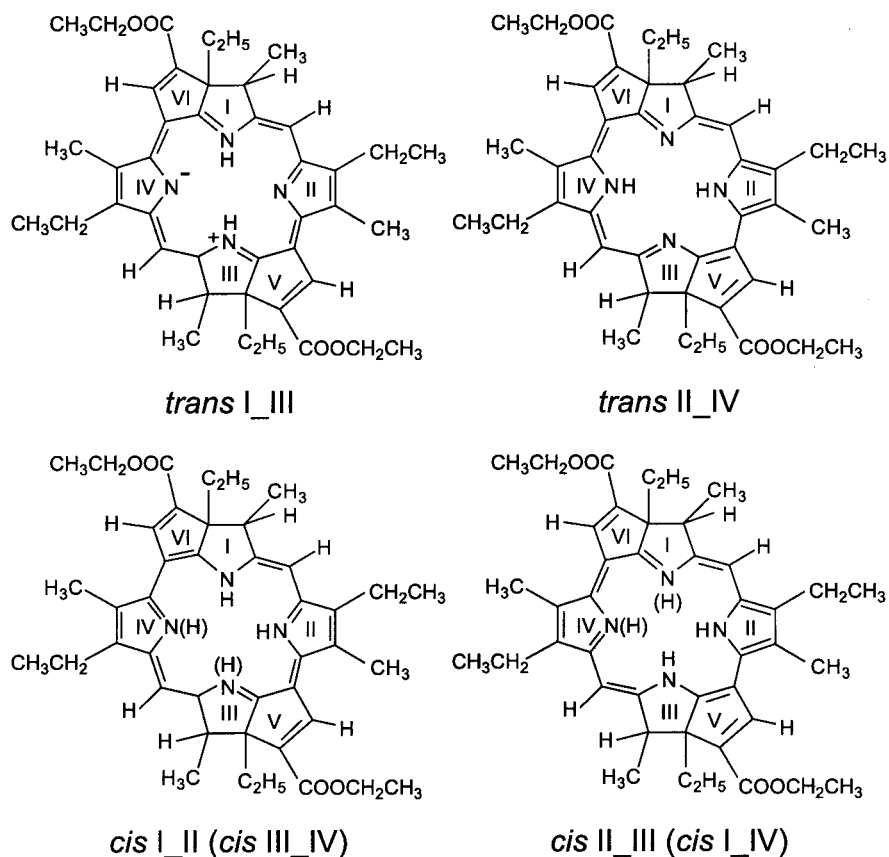
Figure 1. Molecular structures of the possible tautomers of **BP**. The trans II_IV tautomer is seen in the X-ray structure and the liquid-phase NMR spectrum of **BP** as well as in the EPR and ENDOR spectra of **BP**$^{\bullet+}$. The two pairs of cis tautomers, as well as of the trans II_IV tautomer, are observed in the FDMR and TR-EPR spectra of ^{3}**BP**. The alternative trans I_III tautomer is never observed but is included for completeness.

tion to be the trans II_IV **BP** shown in Figure 1. The molecule exhibits a Q$_y$ transition at 843 nm and is readily oxidized, at 0.39 *V* versus saturated calomel electrode, to a π cation radical with a distinctive EPR spectrum.[15,16] In addition, a high-precision crystal structure unambiguously identified the **BP** and provided the first stereochemical parameters for this new class of expanded BCs. The structure formed the basis for ZINDO (Zerner Intermediate Neglect of Differential Overlap) calculations,[17,18,19] which correctly predicted the optical features of **BP**, as well as for iterative extended Hückel calculations which offered insight into the electron density profile of **BP** and its π cation radical, **BP**$^{\bullet+}$.

In this contribution, we extend the earlier EPR results[15,16] for the π cation radical **BP**$^{\bullet+}$ with an electron–nuclear double resonance (ENDOR) study which, in combination with semiempirical and density functional theory (DFT) molecular orbital (MO) calculations, maps in detail the unpaired spin density profile of the doublet state. These results thus parallel and complement previous ENDOR studies of isolated, photosynthetic chromophores.[20]

Further, for the first time for this new class of photosensitizers, we report the characterization of the photoexcited triplet state, ^{3}**BP**, by both time-resolved EPR (TR-EPR) and optically detected magnetic resonance (ODMR). Four triplets with different zero-field splitting (ZFS) parameters are observed, one of which has a longer lifetime than the other three. They are assigned, with the aid of calculations, to different tautomers in which the two inner N—H protons sit on opposite (trans) or adjacent (cis) pyrrole rings; see Figure 1. Thus, a photoinduced proton transfer occurs in the excited state, as has previously been observed in free-base porphyrin[21,22] and chlorin[23] and as was recently considered theoretically.[24] The difference being

that in this study, for the first time, the cis tautomer was actually observed following photoinduced proton transfer.

2. Methods

2.1. Experimental. *Instrumentation.* Continuous-wave (cw) EPR spectra were recorded on a Bruker 300E spectrometer. cw-ENDOR spectra were recorded using a laboratory-built spectrometer consisting of an AEG-20 electromagnet and a Bruker ER041 MR X-band (9−10 GHz) microwave (mw) bridge. A laboratory-made TM$_{110}$ ENDOR cavity ($Q \simeq 1400$, 1 turn per mm NMR coil) was used for ENDOR measurements. A radio frequency (rf) synthesizer (Hewlett-Packard 8660c) in conjunction with a high-power rf amplifier (ENI A-300) was used to generate the cw B_2 rf field in the TM$_{110}$ ENDOR resonator. Deconvolution of the ENDOR spectra was achieved with the program Compass.[25]

TR-EPR spectra were obtained using the laboratory-built X-band spectrometer equipped with a Bruker ER 4118X-MD-5W1 dielectric resonator ($Q \simeq 5000$, ~150 ns time resolution) with optical access. TR-EPR signals were directly detected after pulsed laser excitation and, hence, have a nonderivative line shape with a = enhanced absorption and e = emission. A Nd: YAG laser (6 ns pulse width, $\lambda = 532$ nm, 15 mJ/pulse, 10 *Hz* repetition rate) was used as light source. The transient signals were detected with a digital oscilloscope (Tektronix TDS 520A) interfaced to a PC. The temperature was controlled with a laboratory-built helium-flow cryostat.

Fluorescence detected magnetic resonance (FDMR) spectra were obtained using a home-built apparatus described previously.[26] The detection wavelength was selected by cutoff and band-pass filters (10 nm bandwidths). The excitation was

EPR of Bacteriopurpurin

J. Phys. Chem. B, Vol. 106, No. 10, 2002 **2771**

supplied by a tungsten lamp (250 W) filtered by a CuSO₄ solution and by an IR filter. All FDMR measurements were performed at 1.8 K. Fluorescence spectra were recorded using the FDMR set-up, but in the absence of a mw field and using a monochromator before the detector.

Materials. **BP** was synthesized as described by Robinson et al.[15,16]

EPR/ENDOR: The π cation radical was generated at a concentration of $\sim 10^{-3}$ M in CH_2Cl_2 under high vacuum (10^{-7} mbar) by oxidation with iodine or AgClO₄. Both methods yield the same optical and EPR spectra.[15]

TR-EPR: **BP** was dissolved at a concentration of 5×10^{-3} M in either toluene or ethanol and sealed under high vacuum (10^{-7} mbar) in the dark.

FDMR: **BP** was dissolved in methyl-tetrahydrofuran previously degassed by several freeze–pump–thaw cycles. A flat bar of poly(methyl methacrylate) (PMMA) was left in the solution overnight at room temperature and under nitrogen atmosphere. By this procedure, **BP** was absorbed in the polymer which became colored. The sample obtained was cut to fit directly the helix of the FDMR setup.

CH_2Cl_2, toluene, ethanol, and methyl tetrahydrofuran were purchased from Merck as extra pure spectrophotometric grade solvents. Iodine was purchased from Aldrich in black beads (99.999%) and handled and stored under argon.

2.2. Computational. Geometry optimizations were performed at the unrestricted Kohn–Sham level[27–29] utilizing the Becke3 hybrid exchange functional[30] combined with the Lee, Yang, Parr correlation functional B3LYP[31,30] as implemented in Gaussian 98,[32] using the 6-31G* basis set throughout (B3LYP/6-31G*). A full geometry optimization of **BP** was not performed, rather the 0.005 Å precision X-ray structure[15] was used for all heavy atoms, and only the positions of the protons were energy-optimized. The resulting structure was used for spin density calculations. A full geometry optimization for free-base BC was performed at the same level of theory.

The DFT calculations of spin densities and isotropic hyperfine coupling constants (hfcs) were performed at the unrestricted Kohn–Sham level using the B3LYP functional in conjunction with the 6-31G* basis set.

Semiempirical restricted Hartree–Fock (RHF) INDO, including spin polarization (RHF-INDO/SP) calculations of spin densities and isotropic hfcs, were based on an approach described previously.[33] The method proceeds in two steps: (1) a calculation of RHF doublet MOs by the half-electron method, followed by (2) a subsequent inclusion of SP effects utilizing an unrestricted Hartree–Fock perturbation treatment.

The ZFS parameters D and E were calculated from triplet wave functions built from RHF-INDO singlet ground-state MOs in the original INDO parametrization[34] and followed by a configuration interaction (CI) treatment covering the twenty energetically lowest single excitations. Molecular Coulomb and exchange integrals required for the evaluation of CI matrix elements were calculated in the INDO frame according to the Ridley and Zerner approach.[17] Matrix elements of the electron–electron dipolar operator in the basis of the valence atomic orbital basis set were restricted to two-center Coulomb-type integrals. These were approximated by replacing atomic charge distributions by point charges according to the recipe of Higuchi.[35]

3. Results and Discussion

3.1. Doublet State. *EPR.* The EPR spectrum of **BP**•⁺ in CH_2Cl_2 recorded at 298 K consists of three broad lines of intensity
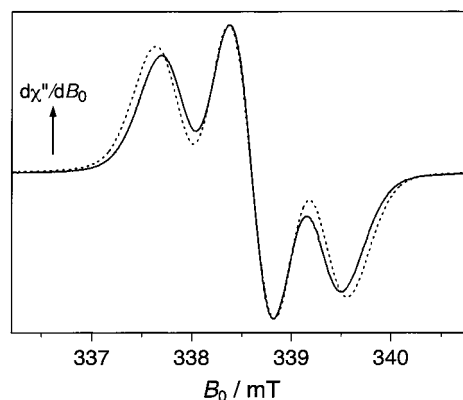

Figure 2. First-derivative EPR spectrum of **BP**•⁺ generated by oxidation of **BP** with iodine in CH_2Cl_2, recorded at 298 K (continuous line). Mw power = 2.01 mW, mw frequency = 9.49 GHz, magnetic field modulation amplitude = 0.044 mT (modulation frequency = 100 kHz). Also shown is a simulation (dotted line) using hfcs (in MHz) from the ENDOR experiments assigned according to the RHF-INDO/SP calculations; see Table 2. 19.39 (2H), 4.39 (6H), 4.01 (2H), 2.90 (2H), 2.15 (4H), 1.63 (2H), 1.01 (2H), 0.78 (2H), and 0.20 (6 H). A Lorentzian line width of 4.65 MHz (0.074 mT) was used.
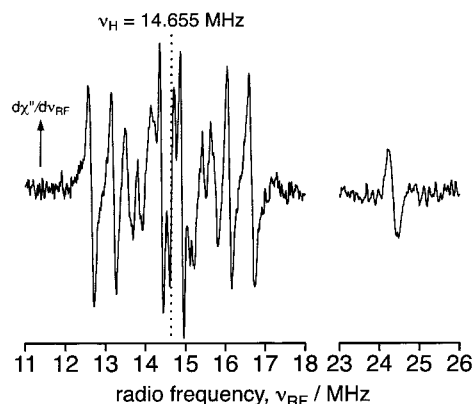

Figure 3. First-derivative cw-ENDOR spectrum of **BP**•⁺ generated by oxidation of **BP** with iodine in CH_2Cl_2, recorded at 298 K. Magnetic field = 344.3 mT, mw power = 2.5 mW, mw frequency = 9.65 GHz, rf power = 200 W, rf modulation frequency = 19 kHz (modulation amplitude = 40 kHz).

ratio 1:2:1 as is expected for the hyperfine pattern arising from two equivalent protons within the **BP** macrocycle, see Figure 2. The spectrum can be simulated using two identical hfcs of 0.650 mT (18.2 MHz) and a line width of 0.27 mT (7.6 MHz) (40% Lorentzian). In previous work this hfc has been assigned to the single β-protons on rings I and III based on MO calculations utilizing the iterative extended Hückel method.[15] The broad EPR line width suggests that additional hfcs are not resolved. We have, therefore, turned to the higher spectral resolution offered by ENDOR spectroscopy.[36]

ENDOR. For doublet state radicals in isotropic solution, two ENDOR lines are expected per hfc at the resonance frequencies

$$\nu_{ENDOR}^{\pm} = |\nu_n \pm \frac{1}{2}a^{iso}| \tag{1}$$

where $\nu_n = g_n\mu_nB_0/h$ is the nuclear Larmor frequency and a^{iso} is the isotropic hfc.

The proton ENDOR spectrum of **BP**•⁺ recorded at 298 K in CH_2Cl_2 reveals nine pairs of lines ranging between 0.2 and 4.4 MHz, see Figure 3. Only the high-frequency component ($\nu^+ = 24.34$ MHz) of the ENDOR line pair corresponding to the large hfc characterizing the EPR spectrum is detected, probably due
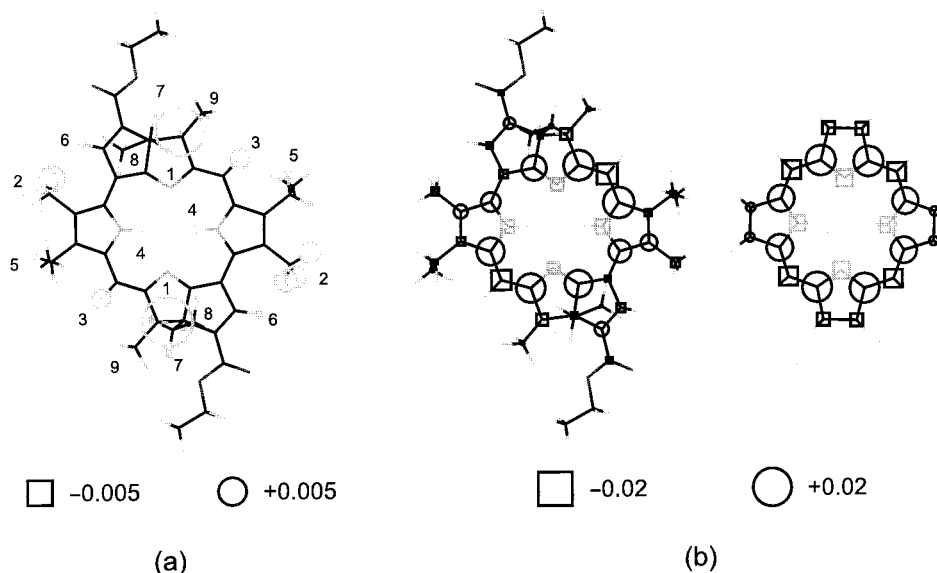
Figure 4. (a) Proton s-spin densities in **BP**•+, calculated using the RHF-INDO/SP approach. The molecular structure was optimized as described in the text. (b) s-spin densities for carbons and nitrogens in **BP**•+ and BC•+ calculated using the RHF-INDO/SP approach. The values are proportional to the area of the circles ($\rho > 0$) and squares ($\rho < 0$). Black is used for carbons, dark gray for nitrogens, and light gray for protons.

TABLE 1: Experimental ¹H Isotropic hfcs (in MHz) for BP•+ Taken from ENDOR Spectrum in Figure 3[a]

ENDOR ¹H hfcs (in MHz)									
19.36	4.39	4.01	2.90	2.15	1.63	1.01	0.78	0.58	0.20

[a] Errors ±0.02 MHz.

to the reduced sensitivity at low frequencies. The experimental proton hfcs are collected in Table 1. The largest hfc of 19.36 MHz is slightly larger (6%) than that determined from the fit of the EPR spectrum (18.2 MHz).

The hfcs at β-protons depend on the unpaired spin density, ρ, at the α-carbon and obey a $\cos^2\theta$ relationship, where θ is the dihedral angle between the p_z orbital at the α-carbon and the β-carbon—proton bond.[37] Therefore, these hfcs are acutely sensitive to conformational changes in the macrocycle. Indeed, the observed large hfcs decrease by a few percent between 300 and 160 K (results not shown) indicating some small structural changes in the saturated pyrrole rings as a function of temperature. Similar temperature effects have been observed[20,38] in BChl a•+ and BPheo a•+. Conformational changes resulting from slightly different concentrations of **BP** or **BP**•+ in solution (i.e., aggregation) or slightly different solvent purity (i.e., water content) might also explain the difference between the hfc determined from the ENDOR experiment and the EPR simulation.

It is of interest to compare the β-proton hfcs to those of related free-base BCs. The β-protons in BPheo a•+ range between 12.6 and 18.8 MHz,[20,38] whereas in the free-base 5,10,15,20-tetraphenylbacteriochlorin cation radical (TPBC•+) these hfcs have been determined at 22.7 MHz by EPR[39] and 23.0 MHz by ENDOR.[40] Thus, a reduction in unpaired spin density and thereby the hfc of the β-protons is observed in molecules containing one or two extra five-membered rings. This is consistent with a delocalization of the unpaired electron over these rings, which alters the unpaired spin density distribution, see below.

To help with the assignment of the other proton hfcs and to compare different theoretical methods, semiempirical and DFT calculations were performed. These calculations were carried out using the crystallographic structure of **BP** (trans II⎯IV tautomer), with the proton positions energy-optimized in the

TABLE 2: Calculated ¹H Isotropic hfcs (in MHz) for BP•+ Calculated Using RHF-INDO/SP and B3LYP/6-31G*[a]

position	multiplicity	RHF-INDO/SP	B3LYP/6-31G*
1	2	21.66	21.18
2	6	4.85	4.45
3	2	3.22	4.76
4	2	0.77	0.93
5	4	0.73	0.41
6	2	0.45	0.44
7	4	−0.34	−0.55
8	6	0.06	0.54
9	6	0.00	0.18

[a] For proton positions, see Figure 4.

cation radical, **BP**•+, using DFT methods. Both yield comparable unpaired spin density distributions and, hence, hfcs for **BP**•+, see Table 2. The unpaired isotropic s-spin densities at the protons calculated by the semiempirical method are depicted in Figure 4a. Both calculations predict that the largest hfc (21.66 MHz from RHF-INDO/SP and 21.18 MHz from B3LYP/6-31G*) arises from the two protons at the β-positions of the saturated rings I and III which probe the unpaired spin density of the α-carbons of those rings.

Figure 4b shows the unpaired s-spin density distribution of the carbons and nitrogens as calculated with the semiempirical method for **BP**•+ and BC•+. The overall spin density profile of **BP**•+, particularly the high spin density at the α-carbons of the pyrrole rings, is typical of that found in BC cation radicals and represents an a_{1u} orbital[41] occupancy for the singly occupied highest MO (the a_{1u} nomenclature, originally developed for porphyrins with D_{4h} symmetry, is traditionally retained for chlorins and BCs). The spin density distribution in **BP**•+ is less symmetric reflecting the lower molecular symmetry, C_{2h}, compared with D_{2h}, in BC•+. A slight delocalization of the unpaired electron spin over the rings V and VI is also evident.

The calculated isotropic hfcs for the β-protons on the reduced ring of BC•+ using semiempirical and DFT methods are 20.07 MHz and 24.92 MHz, respectively. These values fall around the experimental values (22.7−23.0 MHz[39,40]) for TPBC•+. The DFT calculation correctly predicts the trend, i.e., a larger β-proton hfc for BC•+ than for **BP**•+. It is actually slightly too large, but this might also be expected as some spin density is

EPR of Bacteriopurpurin

J. Phys. Chem. B, Vol. 106, No. 10, 2002 **2773**

TABLE 3: Difference in Total Energy (kJ/mol), Pyrrol Proton Separation (Å), and ZFS Parameters D and E (mT) as Calculated for ^{3}BP and Measured by FDMR as Described in the Text

tautomer	total energy	H–H separation	calculated		experimental	
			D	E	$|D|$	$|E|$
trans II_IV	0.0	2.37	23.08	−9.15	24.0 ± 0.2	5.3 ± 0.05
trans I_III	135.5	1.94	20.60	−9.76	−	−
cis I_II	140.6	1.74	26.65	−10.17	27.1 ± 0.2	6.3 ± 0.05
cis III_IV	142.7	1.70	23.64	−9.37	"	"
cis II_III	112.0	1.90	36.02	−7.53	"	"
cis I_IV	108.7	1.89	28.46	−8.54	"	"

delocalized onto the four phenyl groups, thus, slightly decreasing the hfcs in comparison with BC$^{\bullet+}$.

We now turn to the assignment of the other nine experimentally determined hfcs, which are all less than 4.4 MHz. The next two largest hfcs predicted by both methods are the six methyl protons (2) and the two protons at the meso positions (3), see Figure 4a for the numbering scheme. However, the relative magnitude of these hfcs is reversed when comparing RHF-INDO/SP and B3LYP/6-31G*, see Table 3. Thus, unless we choose to trust one method more than the other, unambiguous assignment of these hfcs is not possible at this time.

The remaining calculated hfcs are all less than 1 MHz, although in the experiment hfcs are observed in the range from 0 to 3 MHz. Again, there is no consistent trend between the two methods. Hence, the attribution of the remaining six hfcs is even more difficult because of their small differences.

Nevertheless, if one uses either one of the calculations to make the assignment, it is possible to obtain a good simulation of the EPR spectrum using all 10 hfcs obtained from ENDOR. The simulation shown in Figure 2 was made using the RHF-INDO/SP calculations for assignment. A slightly better fit is possible if one takes the large hfc from the EPR spectrum, but we use all those determined by ENDOR for consistency. Taking into account the nine small hfcs reduces the additional line width needed for the fit from 0.27 mT to 0.074 mT (a 73% reduction). Note that the four nitrogens, which are predicted to have hfcs of −0.084 mT (B3LYP/6-31G*) or −0.065 mT (RHF-INDO/SP), are not included.

In summary, both the semiempirical and DFT calculations predict spin profiles in general agreement with experiment for the large hfcs to the β-protons on rings I and II. This indicates on one hand that DFT can be used successfully for porphyrinic radicals (as has been previously shown by O'Malley[42]) and, on the other hand, that less computer intensive INDO calculations, which have been used extensively for photosynthetic chromophores[33,20] in vitro and in vivo, work quite well. However, the agreement between the calculated and experimental values for the remaining hfcs is rather poor. One reason for this might be that the calculations were based on the singlet ground state structure derived from X-ray crystallography. In the crystal, the molecules pack in pairs with rings I and II partially overlapping rings II and I, respectively, of an inversion-related molecule. The mean plane separation of only 3.61 Å is indicative of $\pi-\pi$ interactions, which can also affect the structure. Conformational differences have been observed between the X-ray crystal structures of porphyrins and their cation radicals.[43,44] Further structural changes are also possible in going from single crystals to solution. Experiment[41,45−47] and calculations[48,49] have also shown that hfcs are solvent-dependent. While the calculations presented here have been performed in vacuo, the EPR/ENDOR experiments were performed in CH$_2$Cl$_2$, a rather polar solvent.

3.2. Triplet State. PDT depends on the presence of a photosensitizer, molecular oxygen, and light to generate reactive
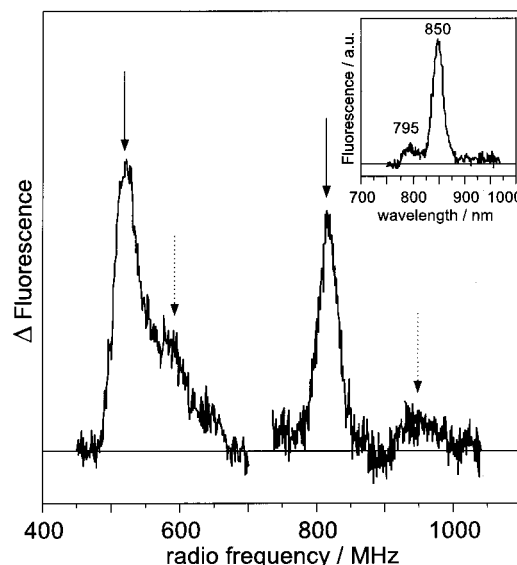

Figure 5. FDMR spectra of ^{3}**BP** in a PMMA matrix detected with a cutoff filter < 780 nm. Indicated with arrows are the transitions belonging to the two triplet species. One triplet (solid line arrows) has two transitions centered at 522 and 815 MHz. The second (dotted line arrows) has transitions at 586 and 944 MHz. The spectral lines of the second triplet are broadened which indicates the contribution of several species with unresolved differences in D and E. Experimental conditions: $T = 1.8$ K; modulation frequency = 320 Hz; mw power = 800 mW; scan rate = 0.83 MHz/s. Insert: fluorescence spectrum of **BP** in PMMA matrix. Excitation: white light filtered by CuSO$_4$. Emission: cutoff filter < 750 nm; resolution = 9 nm; $T = 1.8$ K.

species that chemically attack diseased tissues. The major mechanism for the production of such toxic transients involves photoactivation of the sensitizer to its singlet excited state. This decays via intersystem crossing (ISC) to its triplet state, which reacts with the ground state triplet of molecular oxygen which, in turn, is converted to highly reactive singlet oxygen. The properties of the triplet states of the photosensitizers are thus of obvious interest, particularly for the new class of **BP** photosensitizers considered here.

FDMR. The fluorescence spectrum of ****BP** in a PMMA matrix taken at 1.8 K is presented in Figure 5 (insert). It was recorded with continuous white light excitation filtered by a CuSO$_4$ solution and detected with a cutoff filter <780 nm. The spectrum exhibits two bands at 795 and 850 nm. The FDMR spectrum observed when detecting the emission changes with a cutoff filter <780 nm is shown in Figure 5. In the 450−700 and 750−1050 MHz mw regions, several broad transitions are observed. We have assigned the signals to the $|D| - |E|$ and the $|D| + |E|$ transitions of two triplet states. The 2$|E|$ transitions were not detected. By varying the wavelength of detection (data not shown), we were able to assign the transitions to two different triplets, as indicated with arrows in Figure 5. One triplet (solid line arrows) has two transitions centered at 522 and 815 MHz, giving $|D_1| = 24.0$ mT and $|E_1| = 5.3$ mT. The second (dashed line arrows) has transitions at 586 and 944 MHz, giving $|D_2| = 27.1$ mT and $|E_2| = 6.3$ mT. The spectral lines of the second triplet are broadened, which indicates the contribution of several species with unresolved differences in $|D|$ and $|E|$. We have also repeated the experiments in CH$_2$Cl$_2$. The results, not shown, were similar but the signal-to-noise ratio was rather poor.

TR-EPR. The evolution of the time-resolved EPR spectrum of ^{3}**BP** in frozen toluene at 120 K is shown in Figure 6. Due to anisotropic ISC, the spectrum is spin-polarized. Usually, the
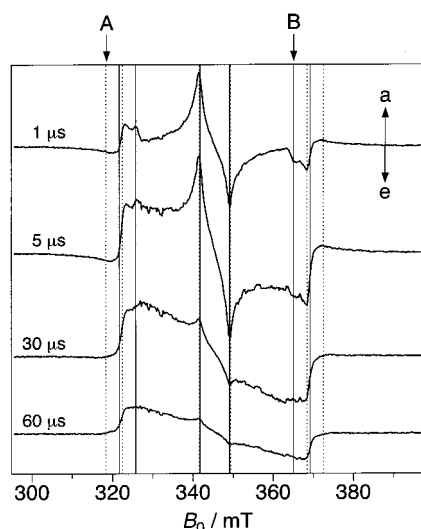
Figure 6. Direct-detected TR-EPR spectra of ^{3}**BP** in toluene recorded at 120 K and at different time delays after the laser pulse. Integration time is 20% of the delay, mw power = 10 mW. The letters a and e stand for absorption and emission, respectively. The spectra consist of contributions of four species, as discussed in the text, three of which are distinguished only by small shifts in *D* and *E*. The vertical (dotted and solid) lines indicate the positions of canonical orientations, as determined by using the *D* and *E* parameters determined from FDMR spectra; see Figure 5. Each set of six lines represents the Z$^-$, Y$^-$, X$^-$, X$^+$, Y$^+$, and Z$^+$ EPR transitions for which the *X*, *Y*, and *Z* axes of the ZFS tensor are parallel to the external magnetic field B_0. A and B indicate the magnetic field positions at which the kinetic traces shown in Figure 7 were recorded.

EPR spectrum of a triplet state shows three pairs of turning points or extrema corresponding to the canonical orientations ($X^\pm$, $Y^\pm$, and $Z^\pm$) of the molecule. The position of these is determined by the ZFS parameters, *D* and *E*, with the separation of the canonical orientations being 2*D*, *D* + 3*E*, and *D* − 3*E*. Inspection of the spectra reveals a more complicated spectral pattern, implying the presence of more than one triplet state, as was observed by FDMR (Figure 5). In Figure 6 are also marked the expected positions of the canonical orientations, using the *D* and *E* values for the two species observed in the FDMR spectrum.

In the spectrum observed at 1 μs after the laser flash, five pairs of turning points are observed in the spectrum with an eaeeaeaaea spectral polarization pattern. For two triplets, the minimum number which is expected from the FDMR results, six pairs would be expected, but probably the very large ae polarized central feature arises from contributions from both species and is, therefore, actually four peaks, occurring at almost the same two magnetic field positions and with the same polarization.

As the spectrum evolves in time, it can be seen that several of the peaks decay much more rapidly than others. This is particularly clear for the outermost ea shoulders, which have completely disappeared after 30 μs. The large central ae peaks also show a rapid intensity decrease. Thus, by 60 μs a typical triplet spectrum with an aaaeee polarization pattern remains. From this spectrum, the ZFS parameters, |*D*| = 24.4 mT and |*E*| = 5.4 mT, may be extracted. These agree well with the smaller pair of values obtained from the FDMR spectrum (|D_1| = 24.0 mT and |E_1| = 5.3 mT). By comparison of the early and late spectra, it is possible to give the polarization pattern of the other species as eeaeaa (see below also).

In summary, in the EPR spectrum of ^{3}**BP** two of the four species are directly observed, with different *D* and *E* values,
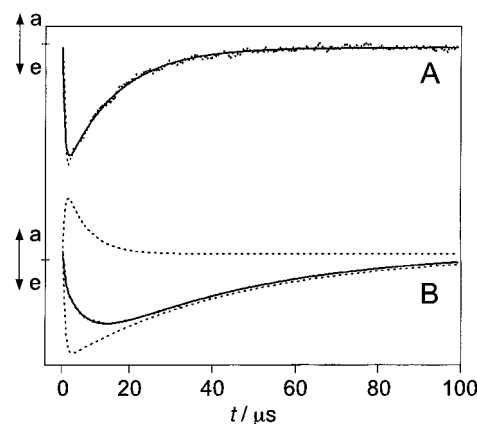

Figure 7. Dots: kinetics of the TR-EPR signals of ^{3}**BP** at the field positions A (B_0 = 319 mT) and B (B_0 = 365 mT) indicated in Figure 6. Dashed lines: simulations for one rising and decaying species using eq 2. The kinetic at field position A can be simulated with one component with k_2 = 0.081 MHz, while the kinetic at field position B consists of the superposition of two contributions with k_{2s} = 0.19 MHz, and k_{2f} = 0.024 MHz. The solid lines represent the final fits. Error margins as estimated by corresponding fits are about 5%.

different spin polarizations and different lifetimes and/or spin−lattice relaxation times.

TR-EPR Spectra and Kinetic Simulations. Figure 7 depicts the time profiles of the TR-EPR spectra recorded at the magnetic field positions A and B indicated in Figure 6. As set out in the Appendix, for the photoreaction $\mathbf{BP} \overset{h\nu}{\rightarrow} {^*}\mathbf{BP} \overset{\text{ISC}}{\rightarrow} {^3}\mathbf{BP} \rightarrow \mathbf{BP}$, the TR-EPR signal may be described by

$$I(B, t) = S(B) \times G(B,t) \qquad (2a)$$

with the time-independent function

$$S(B) = \frac{k_1(B)}{k_3(B)} \qquad (2b)$$

and the time dependent function

$$G(B, t) = \frac{k_3(B)}{k_2(B) - k_3(B)}(e^{-k_3(B)t} - e^{-k_2(B)t})[{^*}\mathbf{BP}]_0 \quad (2c)$$

with the approximation that the recombination rate constants of the triplet sublevels are equal. The initial TR-EPR spectrum in the field domain depends on the initial spin-polarization due ISC and is given by *S*. The TR-EPR kinetics are given by *G*. The solution assumes that the excited singlet state, *BP, is populated instantly after the laser pulse. k_2 includes all possible decay processes, i.e., spin relaxation as well as back reaction to the singlet ground state. k_3^{-1} is essentially the rise time constant of the TR-EPR signal, which, due to the use of an EPR resonator of high *Q*, is determined by the spectrometer time-resolution and is therefore ≤5 MHz. For a detailed explanation of k_1, k_2, and k_3, see Appendix.

The kinetics taken at field position A were simulated with only one paramagnetic intermediate and a monoexponential decay. To simulate the decay at field position B, however, it is necessary to take into account two paramagnetic intermediates with the same rise times (determined by the time resolution of the EPR spectrometer) but different decay rate constants, k_{2s} and k_{2f}, where s stands for slow and f for fast. The overall fit is, therefore, obtained by the sum $S_s \times G_s + S_f \times G_f$, with both parts obeying eq 2.

EPR of Bacteriopurpurin

J. Phys. Chem. B, Vol. 106, No. 10, 2002 **2775**

That at least two paramagnetic intermediates contribute to the TR-EPR spectrum is obvious when comparing the TR-EPR line shapes at different delay times relative to the laser pulse; see Figure 6. The spectrum at later delay times consists only of the contribution of the slowly decaying species, $^3\mathbf{BP}_s$, while the spectrum immediately after the laser pulse consists of a superposition of the fast decaying species, $^3\mathbf{BP}_f$, and the slow decaying species, $^3\mathbf{BP}_s$. At field position B, the EPR signals of $^3\mathbf{BP}_f$ and $^3\mathbf{BP}_s$ have different signs and are, therefore, easy to distinguish from the kinetic traces in Figure 7. At other field positions, in particular in the center of the spectrum, they have the same sign and it is not possible to unambiguously distinguish the two different decay rate constants. Nevertheless, we have tried to separate the contributions of $^3\mathbf{BP}_f$ and $^3\mathbf{BP}_s$ by fitting two field-dependent decay rate constants with significantly different magnitudes for all magnetic field positions.

It should be mentioned that only the outer wings and central peaks of a triplet EPR spectrum can be unambiguously assigned to one specific molecular orientation with respect to the magnetic field. For all other field positions, an overlap of different exponential decays arising from different molecular orientations contributing to the spectrum is expected. It is difficult to distinguish nonmonoexponential decays due to overlap of different orientations from nonmonoexponential decays due to overlap of spectra from different species. However, given that the spectrum detected directly after the laser pulse contains more than one species, as discussed above, and that the spectrum at later times represents a typical triplet spectrum, it is plausible that the two different decay profiles are due to the two different species.

The values of S_s and S_f are plotted over the magnetic field range in spectra a and b of Figure 8 as solid lines and can be assigned to the spectral line shapes of the two species $^3\mathbf{BP}_s$ and $^3\mathbf{BP}_f$, respectively. As mentioned above, the separation works quite well for field positions at which the polarizations of the TR-EPR signals of the two species are different, while for the center region, the deconvolution is not unambiguous. Correspondingly, error margins in the center are rather large compared to those at the spectral wings. It is nevertheless gratifying that the fits produce two spectra with correct spin polarization patterns: aaaeee and eeaeaa, in spectra a and b, respectively, of Figure 8, as deduced by inspection of the TR-EPR spectra in Figure 6; see above.

The two line shapes in Figure 8a,b are simulated as triplet spectra (broken lines) with different ZFS parameter values $|D|$ and $|E|$ using second-order perturbation theory.[50] The spectrum of $^3\mathbf{BP}_s$ can be simulated using $|D_s| = 24.4$ mT and $|E_s| = 5.4$ mT and a relative spin polarization of p_x: p_y: $p_z = 0.23{:}0.04{:}0.73$, Figure 8a. These values compare well with the values $|D_1|$ and $|E_1|$ obtained from FDMR (solid line arrows in Figure 5). The spectrum for $^3\mathbf{BP}_f$, however, cannot be simulated as a spectrum of one triplet state with well-defined D and E values. Rather, it was necessary to include a minimum of three species with the same relative spin polarization p_x: p_y: $p_z = 0.0{:}0.7{:}0.3$, but with different $|D_f|$ values (32.7, 26.6, and 19.9 mT) and $|E_f|$ values (7.4, 6.3, and 4.8 mT), Figure 8b. In fact, D and E are more likely to be distributed over a wide range, as seen in the FDMR spectrum for this species (dotted arrows in Figure 5). A comparison of the simulation with the experimental spectrum obtained 1 μs after the laser pulse (Figure 6) is shown in Figure 8c. The simulation consists of a superposition of simulations in Figure 8a and 8b. It should be mentioned that it
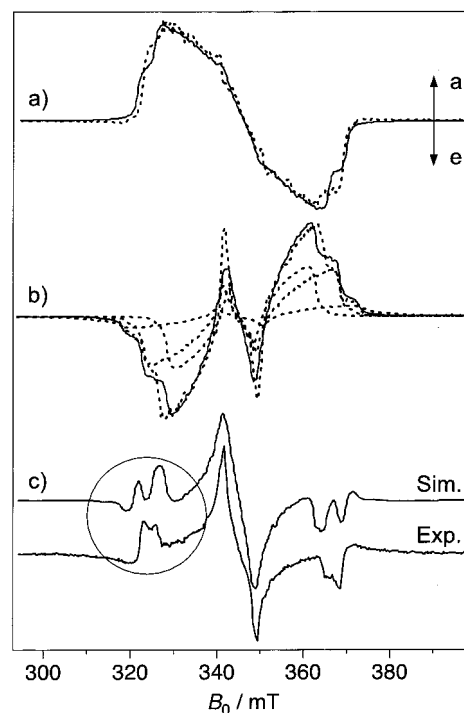

Figure 8. Spectra a and b (solid lines) are the result of a deconvolution of the TR-EPR spectrum of $^3\mathbf{BP}$ shown in Figure 6. They were separated by their different decay constants: a shows the slowly decaying spectral contributions (S_s) and b the fast decaying spectral contributions (S_f). The dotted lines show the fits to these spectra. The spectrum a can be well simulated as a triplet spectrum of one species, while the spectrum b consists of the contribution of three species with different D and E values. (spectrum c) Sum of the fits depicted in spectra a and b, compared to the experimental spectrum recorded 1 μs after the laser pulse. For details, see text.

is particularly difficult to simulate the peaks at the wings of the spectrum (see patterns in circle), which the simulation, Figure 8c, does quite well.

Structural Optimizations. Figure 1 shows the structures of the possible tautomers of **BP**. Although the pairs of cis tautomers should be chemically equivalent, the crystal structure does not show perfect symmetry. Therefore, we have considered both the cis I__II and cis III__IV and the cis II__III and cis I__IV structures, as well as the two nonequivalent trans tautomers, trans I__III and trans II__IV, for our calculations. The energy optimizations were performed on the lowest excited triplet state of **BP** and only the proton positions were optimized, while the heavy atoms were those from the X-ray data.

Table 3 lists the total energies calculated using DFT theory. As expected, trans II__IV, which is derived from the X-ray data,[15] has the lowest total energy. The other three possible structures, trans I__III, cis I__II (III__IV), and cis II__III (I__IV) are energetically more than 100 kJ/mol less favorable. This large energy difference rules out the possibility of thermal activation of structures other than trans II__IV at ambient temperatures ($kT \approx 2.5$ kJ/mol at RT).

The trans II__IV configuration also has the largest distance (2.4 Å) between the N−H protons, thus reducing proton−proton repulsion to a negligible level. The other possible tautomers have far shorter proton−proton distances. Indeed, for the cis I__II (III__IV) tautomers, the adjacent nitrogen atoms are so close that if the protons were in the molecular plane, they would have a separation of only ~1.4 Å. To reduce the repulsion, they are forced out of this plane, thus increasing the separation to ~1.7 Å.

ZFS Calculations. In Table 3 are shown the ZFS parameters D and E calculated using the proton-only optimized geometries of ^{3}**BP**. The trans II_IV has $D = 23.08$ mT, which fits reasonably well with the long-lived species observed in the EPR spectra, $|D_s|$, and the stronger transition seen in the FDMR spectrum, $|D_1|$. The ZFS calculations predict that the alternative trans I_III species has, on the other hand, a smaller value of $D = 20.60$ mT. All four cis structures have larger values of D, spread over a wide range. Although the total energy and proton−proton separation are similar for the two alternative C_2 symmetry related pairs of cis structures, their D values are surprisingly different. This is an interesting demonstration of how a small geometrical difference can have a large effect on the ZFS.

The magnitudes of E from the calculations are all quite similar, and much larger than the experimental values. This is perhaps not surprising, as E is the difference between two large components of the dipole−dipole coupling tensor, and it is very sensitive to small structural changes. We will, therefore, not consider it further here as a guide to assignment.

Discussion of Tautomerism. In the literature, there are two main categories of cis-trans tautomerism discussed in relation to the photoexcited triplet state of free-base porphyrin and its derivatives. Almost exclusively, the trans tautomer is the ground state, and the cis tautomer is only present as an intermediate following a single intramolecular proton transfer. Following this, a second intramolecular proton transfer occurs, which gives the original or a chemically equivalent trans tautomer.

In molecules such as porphycene, fast intramolecular proton transfer was observed even down to 107 K by ^{15}N cross-polarization magic-angle-spinning NMR experiments.[51] Hence, whether the ground-state structure was cis or trans could not be established. A temperature dependence of tautomerism was, however, seen in the TR-EPR spectrum of the triplet state,[52,53] and by an ENDOR and DFT study at liquid helium temperatures, the trans tautomer was shown to be the ground state.[54] At temperatures above 160 K, trans−cis−trans tautomerism occurs on a time scale faster than the TR-EPR time scale, resulting in the observation of an average structure. At intermediate temperatures the TR-EPR spectrum showed the presence of two species: the trans and a short-lived species assigned to the cis tautomer, although recent DFT calculations[55] point to an almost activationless cis−trans interconversion, so the cis tautomer would be expected to have only a momentary existence.

In contrast, the porphyrin intramolecular proton transfer is frozen out below ∼260 K in the ground state[51] but, at lower temperatures, does occur following laser excitation in both porphyrin[21,22] and chlorin.[23] The cis tautomer is not observed, and the laser-induced process is temperature independent in the range 1.3−77 K.[22] The two trans tautomers would be equivalent and indistinguishable if it were not for the presence of the crystal field of the *n*-octane Shpol'skii matrix, which allows both species to be resolved in the ODMR experiment. DFT calculations[24] predict that following excitation from the singlet ground state, ISC brings the porphyrin molecule into the second lowest triplet state, T_2 ($^3B_{1u}$). It then undergoes trans-cis tautomerism on the triplet potential energy surface. Cis−trans tautomerism reaction is predicted to occur primarily on the $^3A'$ potential energy surface and produces the lowest excited triplet state T_1 ($^3B_{2u}$), which is then observed.

For **BP**, no difference between the TR-EPR spectra was observed in the range 10−180 K, so we can discount the possibility of thermal activation, as is observed in porphycene. Following light excitation of **BP** four triplet species are observed, one with a D value corresponding to the ground-state

configuration, the trans II_IV tautomer, and three with larger D. From the calculated values of D, the three latter species could be a superposition of the two possible cis tautomers. In a powder spectrum, it is probable that there is a range of slightly different structures, all contributing different D and E values to the spectrum. This is exactly what was needed to simulate, Figure 8b, the short-lived component of the EPR spectrum in Figure 6.

It can be concluded that intramolecular proton transfer occurs in a fraction of the **BP** molecules before they are detected in the lowest triplet state. Both cis tautomers are formed via a one-proton jump, similar to the first step in the tautomerism process for porphyrin.

In contrast to porphyrin, however, in which the second proton transfer always returns the molecule to the ground state trans, in **BP** the second proton transfer could potentially lead to either the trans II_IV tautomer or the trans I_III tautomer; see Figure 1. Given the calculated 135.5 kJ/mol energy difference between them, we consider it likely that back proton transfer, accompanied by ISC, occurs exclusively to the singlet ground state trans II_IV tautomer.

That the cis tautomer was actually observed in this study is unusual. Presumably, the activation energy for the back proton transfer, cis-trans tautomerism, is quite large compared to that for porphyrin and chlorin, so its lifetime is prolonged enough (10 μs) to make it observable on the time scale of the EPR experiment. This is still much shorter than for the trans II_IV tautomer, whose triplet state EPR spectrum lasts for longer than 100 μs.

4. Conclusions

In the ENDOR experiment, all 10 proton hfcs of **BP**$^{•+}$ could be determined. The single large hfc shows a 6% discrepancy with that derived from the simulation of the EPR spectrum, whose origin is not clear. In comparison with BC$^{•+}$, the β-protons show a reduction in isotropic hfc similar to that observed in BChl *a* and BPheo *a*, as at the meso position the unpaired spin density is reduced by the presence of the exocyclic rings. Including the small hfcs determined by the ENDOR experiment reduces the overall line width needed for the simulation of the EPR spectrum from 0.27 to 0.074 mT. Semiempirical and DFT calculations correctly predict the large hfc but differ significantly for the small hfcs so that assignment is hindered. The problems of assignment for the other hfcs highlight the need for better calculations, including, for example, a fully DFT-optimized structure and solvent effects. Both are in principle possible but may present computational problems for such a large molecule. On the other hand, we are possibly asking too much from the calculations, in trying to assign so many hfcs with such small differences. Further experiments to help with assignment could include ENDOR at low temperatures, and general- and special-TRIPLE resonance, in conjunction with selective deuteration of protons in the molecule.

In the photoexcited triplet state, ^{3}**BP**, apart from the trans II_IV tautomer three additional species have been observed, which have been assigned to either of the cis tautomers by MO calculations of the ZFS parameters. These species have a much weaker FDMR signal and shorter lived TR-EPR spectrum. The decay time constant of a spin-polarized TR-EPR spectrum may be due to either spin−lattice relaxation or lifetime. There was no temperature dependence of the decay observed from ^{3}**BP**, so we are probably measuring its lifetime, which also explains the relative weakness of the FDMR signal. In this case, the average triplet lifetime is reduced.

EPR of Bacteriopurpurin

J. Phys. Chem. B, Vol. 106, No. 10, 2002 **2777**

It would be interesting to carry out these experiments with longer-wavelength excitation and see if, following excitation to the lowest excited singlet state, the second species is still observed. This would confirm whether the proton transfer occurs during ISC or during relaxation from a higher excited singlet state, although in previous work on intramolecular proton tautomerism in porphyrin, the excitation wavelength made no difference to the EPR spectra of the triplet state.[22]

In combination with the previous structural, optical, and redox data for **BP**, these results begin to offer a full characterization of the molecular and electronic properties of this new class of expanded BCs, as well as extending the existing body of data for chromophores of interest in photosynthesis and photonic devices. The FDMR and TR-EPR results supported by calculations, afford first insight into the excited-state properties of the new compound, properties which are crucial to its potential use in PDT and, possibly, in artificial photosynthetic devices.

Appendix

Effect of Spin Lattice Relaxation and Recombination on Spin-Polarized Triplet EPR Signals. To interpret the TR-EPR results and the observed signal decays in section 3.2, we have to consider the system of differential equations for the populations of the photoexcited singlet state and the three triplet sublevels:

$$\frac{\partial[*\textbf{BP}]}{\partial t} = -[2k_{r\pm} + k_{r0}][*\textbf{BP}] \quad (3a)$$

$$\frac{\partial[T_+]}{\partial t} = k_{r\pm}[*\textbf{BP}] - k_{d\pm}[T_+] - k_{rel}([T_+] - [T_0]) - \\ k_{rel\pm}([T_+] - [T_-]) \quad (3b)$$

$$\frac{\partial[T_0]}{\partial t} = k_{r0}[*\textbf{BP}] - k_{d0}[T_0] - k_{rel}([T_0] - [T_+]) - \\ k_{rel}([T_0] - [T_-]) \quad (3c)$$

$$\frac{\partial[T_-]}{\partial t} = k_{r\pm}[*\textbf{BP}] - k_{d\pm}[T_-] - k_{rel}([T_-] - [T_0]) - \\ k_{rel\pm}([T_-] - [T_+]) \quad (3d)$$

where $k_{r\pm}$ and k_{r0} are the ISC rate constants and therefore the populating rate constants and $k_{d\pm}$ and k_{d0} are the recombination rate constants of the corresponding triplet sublevels $|T_\pm\rangle$ and $|T_0\rangle$, respectively. In a general case, all these rate constants can

be different and may be dependent on the magnetic field. k_{rel} is the one-quantum relaxation rate constant, and $k_{rel\pm}$ is the double quantum relaxation rate constant. *BP denotes the excited singlet state, and the brackets denote the concentration (in the case of *BP) or population (in the case of the triplet sublevels).

The population and recombination rate constants for the high-field triplet states are given by the product of the respective proportion of the zero-field triplet states on the high field function and the decay rate constants for the three zero-field sublevels. Therefore, at high magnetic field, the population and decay rate constants for $|T_+\rangle$ and $|T_-\rangle$ are equal. At high temperatures, one can neglect also the spin polarization due to Boltzmann equilibrium and, therefore, $[T_+] = [T_-]$. In this case, double quantum relaxation, with a rate constant, $k_{rel\pm}$, has no effect, and it will be neglected.

There exist two limiting cases for which one can easily solve this system analytically: (i) When $k_{d\pm} = k_{d0}$, the recombination does not generate additional spin polarization, and the EPR signal of one species can be described by using eq 2. (ii) When $k_{rel} = 0$, the EPR signal is given by the difference of two populations each following eq 2 but with different rate constants. In the following, we derive the solutions for the two cases.

(i) $k_{d\pm} = k_{d0}$. It is convenient to reformulate eqs 3a–d using the EPR intensity of the $|T_+\rangle \leftrightarrow |T_0\rangle$ transition, $I = [T_+] - [T_0]$, and $[T_+] = [T_-]$:

$$\frac{\partial[*\textbf{BP}]}{\partial t} = -[2k_{r\pm} + k_{r0}][*\textbf{BP}] \quad (4a)$$

$$\frac{\partial I}{\partial t} = (k_{r\pm} - k_{r0})[*\textbf{BP}] - (k_d + 3k_{rel})I \quad (4b)$$

with $k_d = k_{d\pm} = k_{d0}$. The solution of this system of equations is

$$[*\textbf{BP}](t) = [*\textbf{BP}]_0 \times e^{-k_3 t} \quad (5a)$$

$$I(t) = \frac{k_1}{k_2 - k_3} (e^{-k_3 t} - e^{-k_2 t})[*\textbf{BP}]_0 \quad (5b)$$

with $k_1 = k_{r\pm} - k_{r0}$, $k_2 = k_d + 3k_{rel}$, and $k_3 = 2k_{r\pm} + k_{r0}$. $I(B,t)$ may be written as

$$I(B,t) = S(B) \times G(B, t) \quad (6a)$$

with the time-independent function

$$S(B) = \frac{k_1(B)}{k_3(B)} \quad (6b)$$

and the time-dependent function

$$G(B, t) = \frac{k_3(B)}{k_2(B) - k_3(B)}(e^{-k_3(B)t} - e^{-k_2(B)t})[*\textbf{BP}]_0 \quad (6c)$$

The quantity $S(B)$ describes the spin polarization of the two states if there were no decay of the triplet sublevels and *BP has transferred its population totally to $|T_+\rangle$, $|T_0\rangle$, and $|T_-\rangle$, i.e., $S(B) = I(t\to\infty, k_2=0)$ is the initial TR-EPR signal. It is a field dependent but time independent quantity.

$I(B,t)$ is the expression used in eq 2 in section 3.2. It should be mentioned that for this case monoexponential decays are expected even when both relaxation and recombination contribute with different rate constants to the decay of the spin polarization.

(ii) $k_{rel} = 0$. Neglecting relaxation, it is possible to solve eqs 3b and 3c separately:

$$[*\mathbf{BP}](t) = [*\mathbf{BP}]_0 \times e^{-k_3 t} \tag{7a}$$

$$[T_+] = \frac{k_{r\pm}}{k_{d\pm} - k_3} (e^{-k_3 t} - e^{-k_{d\pm} t})[*\mathbf{BP}]_0 \tag{7b}$$

$$[T_0] = \frac{k_{r0}}{k_{d0} - k_3} (e^{-k_3 t} - e^{-k_{d0} t})[*\mathbf{BP}]_0 \tag{7c}$$

with the rate constants as given for eq 5 In this case, the EPR signal is proportional to

$$I(B,t) = [T_+] - [T_0] =$$
$$\left[\frac{k_{r\pm}}{k_{d\pm} - k_3} (e^{-k_3 t} - e^{-k_d t}) - \frac{k_{r0}}{k_{d0} - k_3} (e^{-k_3 t} - e^{-k_{d0} t}) \right][*\mathbf{BP}]_0 \tag{8}$$

From the spectral decay alone in section 3.2, one cannot decide whether the EPR signal consists of two spectral contributions each following eq 6 or only one following eq 8. However, as discussed in section 3.2, the initial spectrum in Figure 6 is not the typical spectrum of a single triplet state but must consist of at least two species. Taking this into account, it is a reasonable first approach to separate the contributions of the two species, using the sum of two species following eq 6, as has been done in section 3.2 (eq 2).

References and Notes

(1) Karrash, S.; Bullough, P.; Ghosh, R. *EMBO J.* **1995**, *14*, 631.

(2) Freer, A.; Prince, S.; Sauer, K.; Papiz, M.; Hawthornthwaite-Lawless, A.; McDermott, G.; Cogdell, R.; Isaacs, N. W. *Structure* **1996**, *4*, 449.

(3) Koepke, J.; Hu, X.; Muenke, C.; Schulten, K.; Michel, H. *Structure* **1996**, *4*, 581.

(4) Li, Y.; Zhou, W.; Blankenship, R. E.; Allen, J. P. *J. Mol. Biol.* **1997**, *271*, 456.

(5) Ermler, U.; Fritzsch, G.; Buchanan, S. K. *Structure* **1994**, *2*, 925.

(6) Deisenhofer, J.; Epp, O.; Sinning, I.; Michel, H. *J. Mol Biol.* **1995**, *246*, 429.

(7) Sternberg, E. D.; Dolphin, D.; Brockner, C. *Tetrahedron* **1998**, *54*, 4151.

(8) Zilberstein, J.; Bromberg, A.; Frantz, A.; Rosenbach-Belkin, V.; Kritzmann, A.; Pferfermann, R.; Solomon, Y.; Scherz, A. *Photochem. Photobiol.* **1997**, *65*, 1012.

(9) Schuitmaker, J. J.; de Koster, B.; Elferink, J. *Photochem. Photobiol.* **1998**, *68*, 841.

(10) Morgan, A. R.; Gupta, S. *Tetrahedron Lett.* **1990**, *31*, 285.

(11) Gunter, M.; Robinson, B. C. *Aust. J. Chem.* **1990**, *43*, 1839.

(12) Forsyth, T. P.; Nurco, D. J.; Pandey, R. K.; Smith, K. M. *Tetrahedron Lett.* **1995**, *36*, 9093.

(13) Ressler, M. M.; Pandey, R. K. *CHEMTECH* **1998**, *March*, 39.

(14) Pandey, R. K.; Zheng, G. In *The Porphyrin Handbook*; Kadish, K. M., Smith, K. M., Guilard, R., Eds.; Academic Press: New York, 2000; Vol. 6, p 157.

(15) Robinson, B. C.; Barkigia, K. M.; Renner, M. W.; Fajer, J. *J. Phys. Chem. B* **1999**, *103*, 7324.

(16) Robinson, B. C. *Tetrahedron* **2000**, *56*, 6005.

(17) Ridley, J.; Zerner, M. C. *Theor. Chim. Acta* **1973**, *32*, 111.

(18) Ridley, J.; Zerner, M. C. *Theor. Chim. Acta* **1976**, *42*, 223.

(19) Thompson, M. A.; Zerner, M. C.; Fajer, J. *J. Phys. Chem.* **1976**, *95*, 5693.

(20) Lubitz, W.; Lendzian, F.; Scheer, H.; Plato, M.; Möbius, K. *Appl. Magn. Reson.* **1997** *13*, 531.

(21) van Dorp, W. G.; Shoemaker, W. H.; M., S.; van der Waals, J. H. *Mol. Phys.* **1975**, *30*, 1701.

(22) Völker, S.; van der Waals, J. H. *Mol. Phys.* **1976**, *32*, 1703.

(23) van der Bent, S. J.; Schaafsma, T. J. *J. Chem. Phys.* **1977**, *68*, 1857.

(24) Nguyen, K. A.; Pachter, R. *J. Phys. Chem. A* **2000**, *104*, 4549.

(25) Tränkle, E.; Lendzian, F. *J. Magn. Res.* **1989**, *84*, 537.

(26) Carbonera, D.; Giacometti, G.; Agostini, G. *App. Magn. Res.* **1992**, *3*, 859.

(27) Barone, V. *J. Phys. Chem.* **1995**, *99*, 11659.

(28) Barone, V. In *Recent Advances in Density-Functional Methods*; Chong, D. P., Ed.; World Scientific Publishing: Singapore, 1995; Part I.

(29) Rega, N.; Cossi, M.; Barone, V. *J. Chem. Phys.* **1996**, *105*, 11060.

(30) Becke, A. D. *J. Chem. Phys* **1993**, *98*, 5648.

(31) Lee, C.; Yang, W.; Parr, R. G. *Phys. Rev. B* **1988**, *37*, 785.

(32) Frisch, M. J.; Trucks, G. W.; Schlegel, H. B.; Scuseria, G. E.; Robb, M. A.; Cheeseman, J. R.; Zakrzewski, V. G.; Montgomery, J. A.; Stratmann, R. E.; Burant, J. C.; Dapprich, S.; Millam, J. M.; Daniels, A. D.; Kudin, K. N.; Strain, M. C.; Farkas, O.; Tomasi, J.; Barone, V.; Cossi, M.; Cammi, R.; Mennucci, B.; Pomelli, C.; Adamo, C.; Clifford, S.; Ochterski, J.; Petersson, G. A.; Ayala, P. Y.; Cui, Q.; Morokuma, K.; Malick, D. K.; Rabuck, A. D.; Raghavachari, K.; Foresman, J. B.; Cioslowski, J.; Ortiz, J. V.; Stefanov, B. B.; Liu, G.; Liashenko, A.; Piskorz, P.; Komaromi, I.; Gomperts, R.; Martin, R. L.; Fox, D. J.; Keith, T.; Al-Laham, M. A.; Peng, C. Y.; Nanayakkara, C.; Gonzalez, M.; Challacombe, M.; Gill, P. M. W.; Johnson, B. G.; Chen, W.; Wong, M. W.; Andres, J. L.; Head-Gordon, M.; Replogle, E. S.; Pople, J. A. *Gaussian 98*, Revision A.7; Gaussian, Inc.: Pittsburgh, PA, **1998**.

(33) Plato, M.; Möbius, K.; Lubitz, W. In *Chlorophylls*; Scheer, H., Ed.; CRC Press: Boca Raton, FL, 1990; pp 1015−1046.

(34) Pople, J. A.; Beveridge, D. L. *Approximate Molecular Orbital Theory*; McGraw-Hill: New York, 1970.

(35) Higuchi, J. *J. Chem. Phys.* **1963**, *38*, 1237.

(36) Kurreck, H.; Kirste, B.; Lubitz, W. *Electron Nuclear Double Resonance Spectroscopy of Radicals in Solution*; VCH Publishers: New York, 1988.

(37) McConnell, H. M. *J. Chem. Phys.* **1956**, *24*, 764.

(38) Horning, T. L.; Fujita, E.; Fajer, J. *J. Am. Chem. Soc.* **1986**, *108*, 323.

(39) Fajer, J.; Borg, D. C.; Forman, A.; Felton, R. H.; Dolphin, D.; Vegh, L. *Proc. Natl. Acad. Sci. U.S.A.* **1974**, *71*, 994.

(40) Mössler, H.; Wittenberg, M.; Niethammer, D.; Mudrassagam, R. K.; Kurreck, H.; Huber, M. *Magn. Reson. Chem.* **2000**, *38*, 67.

(41) Fajer, J.; Davis, M. S. In *The Porphyrins*; Dolphin, D., Ed.; Academic: New York, 1979; Vol. IV.

(42) O'Malley, P. J. *J. Am. Chem. Soc.* **1999**, *121*, 3185.

(43) Renner, M. W.; Barkigia, K. M.; Zang, Y.; Medforth, C. J.; Smith, K. M.; Fajer, J. *J. Am. Chem. Soc.* **1994**, *116*, 8582.

(44) Renner, M. W.; Barkigia, K. M.; Fajer, J. *Inorg. Chim. Acta* **1997**, *263*, 181.

(45) Joela, H.; Lehtovuori, P. *Phys. Chem. Chem. Phys.* **1999**, *1*, 4003.

(46) Steinhoff, H.-J.; Savitsky, A.; Wegener, C.; Pfeiffer, M.; Plato, M.; Möbius, K. *Biochim. Biophys. Acta* **2000**, *1457*, 253.

(47) Kawamura, T.; Matsunami, S.; Yonezawa, T. *Bull. Chem. Soc. Jpn.* **1967**, *40*, 1111.

(48) Barone, V. *Chem. Phys. Lett.* **1996**, *262*, 201.

(49) Weber, S.; Richter, G.; Schleicher, E.; Bacher, A.; Möbius, K.; Kay, C. W. M. *Biophys. J.* **2001**, *81*, 1195.

(50) Atherton, N. M. *Principles of Electron Spin Resonance*; Ellis Horwood: Chichester, U.K., 1993.

(51) Wehrle, B.; Limbach, H.-H.; Köcher, M.; Ermer, O.; Vogel, E. *Angew. Chem.* **1987**, *99*, 914.

(52) Kay, C. W. M.; Möbius, K. *Mol. Phys.* **1998**, *95*, 1013.

(53) Kay, C. W. M.; Elger, G.; Möbius, K. *Phys. Chem. Chem. Phys.* **1999**, *1*, 3999.

(54) Kay, C. W. M.; Gromadecki, U.; Törring, J. T.; Weber, S. *Mol. Phys.* **2001**, *99*, 1413.

(55) Kozlowski, P. M.; Zgierski, M. Z.; Baker, J. *J. Chem. Phys.* **1998**, *109*, 5905.